Chemical Science

ROYAL SOCIETY OF CHEMISTRY

EDGE ARTICLE

View Article Online
View Journal

Cite this: DOI: 10.1039/d5sc08033a

All publication charges for this article have been paid for by the Royal Society of Chemistry

Unveiling the electron–phonon coupling anisotropy in 2D covalent organic frameworks

Yilin Zhang,[a] Zhixiang Dai,[a] Zihan Tan,[a] Hongli Yang,[be] Chao Xu,[c] Shengyang Zhou *[ae] and Zhong-Ming Li [bde]

Covalent organic frameworks (COFs) are emerging organic semiconductors with potential for energy conversion and storage. However, their electronic structure and electron–phonon interactions remain poorly understood. This issue is particularly important in 2D COFs, where covalent and van der Waals interactions along orthogonal directions manifest intrinsic anisotropy. In this work, six 2D COFs with varied bond linkages, stacking patterns, and side-group conjugation were synthesized to investigate their electron–phonon interaction properties. The results show that electron–phonon coupling (EPC) exhibits obvious direction dependence. Strong EPC is observed along the interlayer direction, whereas negligible momentum exchange occurs along the in-plane direction. A positive correlation between thermal conductivity and EPC strength was recognized, in contrast to the behavior of conventional semiconductors. Further analysis confirms that interlayer EPC hardens phonon frequencies and promotes in-plane acoustic phonon bunching, thereby enhancing thermal transport. A proof-of-concept study using a highly oriented COF film revealed extreme transport anisotropy. The thermal conductivity difference between perpendicular directions approaches two orders of magnitude, while the in-plane value reaches 20 W m^{-1} K^{-1} as determined by the laser flash method. These findings provide fundamental insight into the transport mechanism of 2D COFs and highlight their potential as efficient thermal conductors.

Received 17th October 2025
Accepted 16th December 2025

DOI: 10.1039/d5sc08033a

rsc.li/chemical-science

Introduction

Covalent organic frameworks (COFs) possess versatile and tunable molecular architectures with intrinsic porosity, which already confer notable advantages in gas storage,[1–5] molecular separation,[6,7] and heterogeneous catalysis.[8–11] More recently, their semiconducting features have attracted considerable attention. In particular, two-dimensional (2D) COFs show distinctive electronic characteristics, positioning them as promising candidates for energy conversion and storage applications, such as photocatalysis.[12–15] As organic semiconductors, 2D COFs exhibit unique structural traits compared with other known organic systems. Their high crystallinity ensures ordered atomic arrangements that strongly influence electronic band structures and charge transport, providing a degree of structural precision not usually attainable in polymer-based semiconductors. In addition, 2D COFs display intrinsic anisotropy: within each plane, covalent linkages dominate, while adjacent layers are held by van der Waals interactions.[16–18] Moreover, the frameworks can be tailored at the molecular level, offering flexible strategies to tune electronic properties. Despite these promising aspects, the understanding of the electronic structures of 2D COFs and their interaction with lattice vibrations remains limited. This lack of knowledge prevents the establishment of predictive theoretical models to guide molecular design for semiconductor-related applications. A deeper comprehension of these interactions is also essential for exploiting their full potential in determining thermal, electrical, magnetic, and optical properties, which would enable advances in microelectronics, thermal management, and light-matter coupling.

Herein, we report the design and synthesis of six representative 2D COFs that differ in covalent linkages (imine and keto-enamine), stacking patterns (AA and AB), and side-group polarity (electron-donor and electron-acceptor). Using high-resolution spectroscopy techniques combined with low-temperature approaches, we systematically investigated their electron and phonon structures. Our study reveals pronounced anisotropy. Along the interlayer *c* axis, where van der Waals forces dominate, electron–phonon coupling (EPC) leads to the

[a]College of Materials Science and Engineering, Sichuan University, Chengdu 610065, China. E-mail: shengyang.zhou@scu.edu.cn

[b]College of Polymer Science and Engineering, Sichuan University, Chengdu 610065, China

[c]Department of Materials Science and Engineering, The Ångström Laboratory, Uppsala University, Uppsala 752 37, Sweden

[d]West China Hospital/West China School of Medicine, Sichuan University, Chengdu 610041, China

[e]State Key Laboratory of Advanced Polymer Materials, Sichuan University, Chengdu 610065, China

formation of quasi-large polarons reminiscent of Fröhlich interactions. These excitations strongly affect semiconducting behavior by regulating charge dynamics and phonon modes. In contrast, in the *ab* plane stabilized by covalent bonds, momentum exchange between electrons and phonons is minimal. This anisotropy produces the unusual trend that thermal conductivity increases with EPC strength. First-principles calculations confirm that stronger EPC stiffens phonon frequencies and induces bunching of in-plane acoustic phonons, thereby facilitating thermal transport. To validate these predictions, we measured the thermal conductivity of a highly oriented 2D COF film with layered stacking. The ratio of in-plane to cross-plane conductivity approaches two orders of magnitude, and the in-plane value reaches around 20 W m^{-1} K^{-1} as measured by the laser flash method, far exceeding isotropic powders and most polymeric materials. These findings demonstrate the essential role of anisotropic EPC in enhancing in-plane heat transport. This work offers new insight into electron–phonon interactions in COFs and provides a basis for future exploration of their unique physicochemical properties and broader functional applications.

Results and discussion

Using one of the most representative imine-linked 2D COFs, TFB-DB (also known as LZU-1),[19] as a model system, we investigated how different crystalline stacking modes influence the electronic structure. Through a one-step aqueous synthesis, we obtained highly crystalline TFB-DB polycrystalline powder with classical AA stacking at room temperature (Fig. 1a and S1). When the solution was heated to 80 °C, we obtained highly crystalline TFB-DB polycrystalline powder adopting the AB stacking configuration (Fig. 1b and S2). To the best of our knowledge, this represents the first successful preparation of AB-stacked 2D TFB-DB. This aqueous approach provides a practical route to control stacking arrangements of 2D COFs and establishes a reliable material basis for studying the correlation between stacking and electronic properties. As illustrated in Fig. 1c, the high-resolution diffuse reflectance ultraviolet-visible (DR UV-vis) spectrum of TFB-DB-AA displays two distinct absorption bands. The band near 350 nm mainly originates from interlayer π–π conjugation, whereas the broad absorption across 400–600 nm is attributed to the extended conjugation between alternating imine and benzene units within the in-plane framework.[20] To validate these assignments, we carried out DFT-based optical absorption calculations using optimized COF structures. The simulated spectra of TFB-DB agree well with the experimental data, reproducing both the sharp band at 300–400 nm and the extended absorption above 400 nm (Fig. S3). Analysis of the dielectric tensor along different crystallographic directions indicates that the higher-energy band arises from interlayer π–π* transitions along the *c*-axis, while the lower-energy absorption originates from intralayer conjugated transitions. This interpretation aligns with numerous previous studies. As summarized in Table S1 (SI), both theoretical and experimental results consistently support that the 300–400 nm band is due to interlayer transitions, whereas absorption beyond 400 nm arises from intralayer conjugation.

Compared with the AA stacking mode, AB stacking enhances the intensity of the interlayer conjugation absorption and slightly narrows the extended absorption range to about 500 nm (Fig. 1d). This result suggests that AB stacking enhances the interlayer coupling of TFB-DB through direct interactions between adjacent layers, while the A–B–A pathway may also contribute to the coupling, potentially leading to a modest increase in the band gap. The absorption edge intensity for both AA and AB stacking shows an initial sharp drop followed by a gradual attenuation. Similar behavior has been observed in many other 2D COFs, suggesting the possible coexistence of direct and indirect band gaps.[21–24] Mathematical fitting of the absorption edge with the Tauc relation yielded a good linear dependence for $h\nu$ *versus* $(\alpha h\nu)^2$ as well as $(\alpha h\nu)^{1/2}$, providing preliminary evidence that TFB-DB COFs may contain both direct and indirect band gaps (Fig. S4 and S5).[25,26] To evaluate the reliability of the optical band gaps obtained from the Tauc analysis, we compared them with electronic band gaps calculated by DFT based on optimized COF structures. As shown in Fig. S6 and S7, the calculated gaps are slightly smaller due to the idealized assumptions of the models, yet the overall trends agree well with the experimental values, confirming the validity of our band gap determination.

To further confirm the coexistence of direct and indirect band gaps in TFB-DB, photoluminescence (PL) excitation spectra were collected at room temperature (Fig. S8). The results indicate that excitation light with wavelengths below 400 nm produces only weak photoluminescence signals, whereas excitation light above 450 nm generates markedly stronger emission. This behavior suggests that electrons promoted to excited states through interlayer transitions relax mainly through non-radiative pathways, while those excited by in-plane transitions decay through radiative processes. These findings imply that the indirect band gap likely originates from interlayer van der Waals interactions, whereas the direct band gap is associated with in-plane covalent bonding. Furthermore, although the optical absorption range of AB-stacked TFB-DB is narrower, its PL wavelength range closely matches that of AA-stacked TFB-DB, extending up to 800 nm. The AB-stacked sample exhibits a relatively larger Stokes shift, suggesting stronger non-radiative relaxation than in the AA configuration, and this behavior may be influenced not only by adjacent-layer interactions but also by the A–B–A stacking sequence, which could modify the interlayer potential field and enhance out-of-plane electron–phonon coupling.[27,28]

To investigate detailed differences in the electronic structures, temperature-dependent PL spectra of TFB-DB with two distinct stacking modes were collected (Fig. 1e and f). This approach enables the decoupling and analysis of contributions from different fine electronic features. The PL intensity of both samples decreases with increasing temperature; however, the AB-stacked sample shows a faster decay than the AA-stacked sample. The exciton binding energy of the AB-stacked sample (66.21 meV, Fig. S9b) is slightly larger than that of the AA-stacked sample (64.45 meV, Fig. S8b), suggesting a marginally

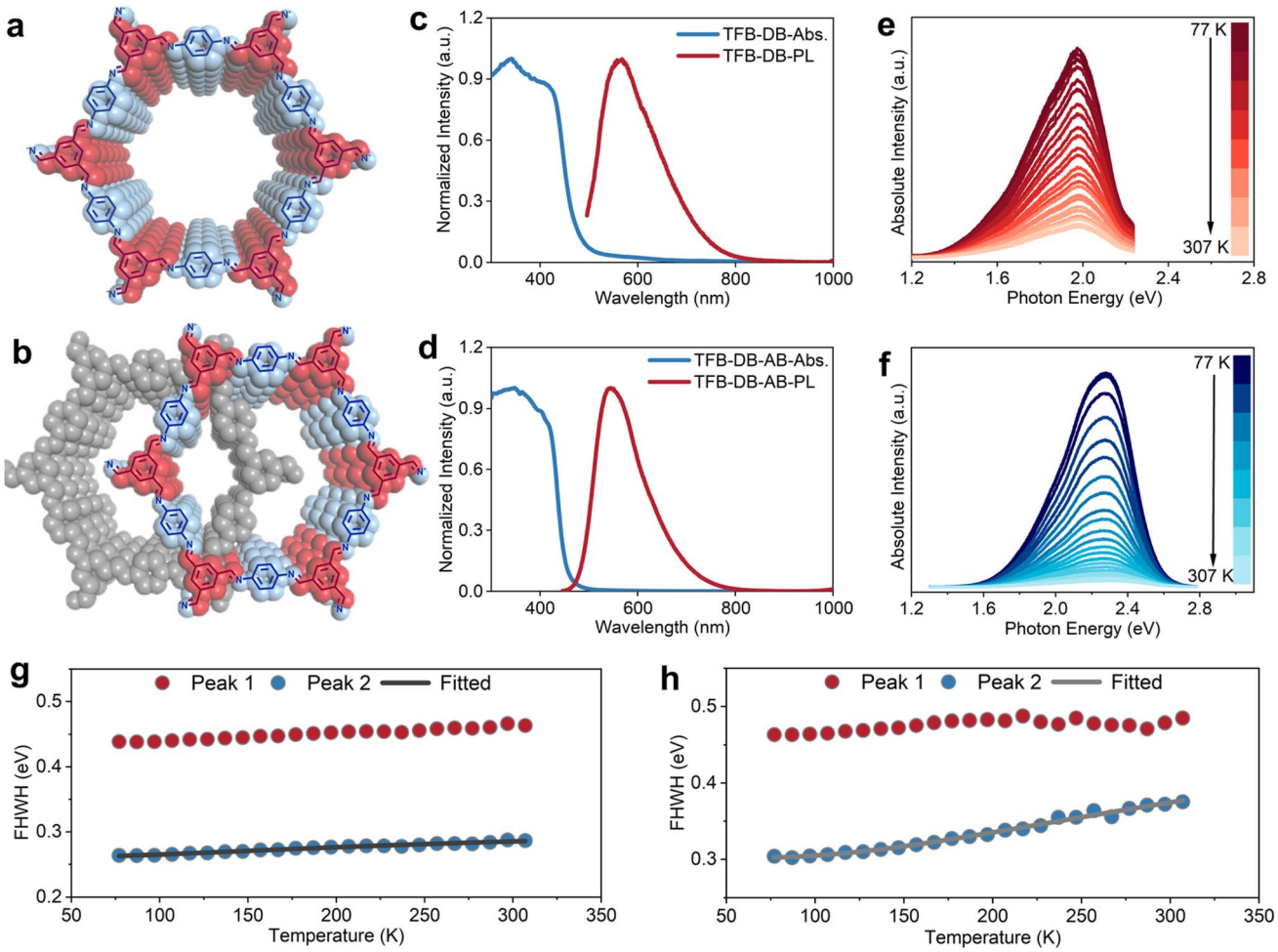

Fig. 1 Molecular structure and spectroscopic characterization of 2D TFB-DB COFs with AA and AB stacking. (a and b) Molecular structures; (c and d) intensity-normalized diffuse reflectance (DR) UV-vis and PL spectra; (e and f) temperature-dependent steady-state PL spectra; (g and h) temperature-dependent FWHM of three representative PL peaks for the AA- and AB-stacked COFs, respectively. The solid gray lines represent fits to the Fröhlich polaronic broadening model, which accounts for contributions from both inhomogeneous broadening and Fröhlich coupling with LO phonons.

weaker charge separation ability in the AB stacking mode. At low temperatures, the PL spectrum of both samples clearly contains two sub-peaks that can be attributed to carrier relaxation and emission through interlayer conjugation (indirect band gap) and intralayer extended conjugation (direct band gap). Gaussian fitting successfully deconvoluted the PL spectrum into these two components. The lower-energy PL peak corresponds to intralayer relaxation, whereas the higher-energy peak originates from interlayer relaxation. The temperature dependence of the full width at half maximum (FWHM) of the two peaks is summarized in Fig. 1g and h. The FWHM of the intralayer PL peak remains nearly constant with rising temperature, while the interlayer PL peak broadens significantly, which is a characteristic signature of EPC.[29,30] Fitting the data with the Fröhlich polaronic broadening model shows that both AA- and AB-stacked samples exhibit coupling between electrons and longitudinal optical phonons. This behavior is consistent with the formation of a Fröhlich-type large polaron and falls within the temperature range over which the Fröhlich model is applicable (Table S2).[31–35] This result suggests the presence of EPC along the interlayer direction in TFB-DB, while EPC within the in-plane direction is negligible. Moreover, the calculated Fröhlich coupling factors (α) reveal stronger EPC in the AB-stacked sample ($\alpha = 0.126$) than in the AA-stacked sample ($\alpha = 0.09$).

On this basis, we incorporated an electron-withdrawing trifluoromethyl group and an electron-donating hydroxyl group into the molecular framework (Fig. 2a, b, S10 and S11) to investigate how side-group polarity influences the electronic structure of 2D TFB-DB. X-ray diffraction (XRD) analysis shows that introducing either hydroxyl or trifluoromethyl substituents results in only minimal changes to the (001) interlayer spacing (Fig. S12), indicating that functionalization does not significantly perturb the stacking distance in these COFs. Consistently, DR UV-vis spectra reveal that these chemical modifications leave the position of the interlayer π–π absorption peak unchanged (Fig. 2c and d). However, the trifluoromethyl group narrows the absorption window, thereby

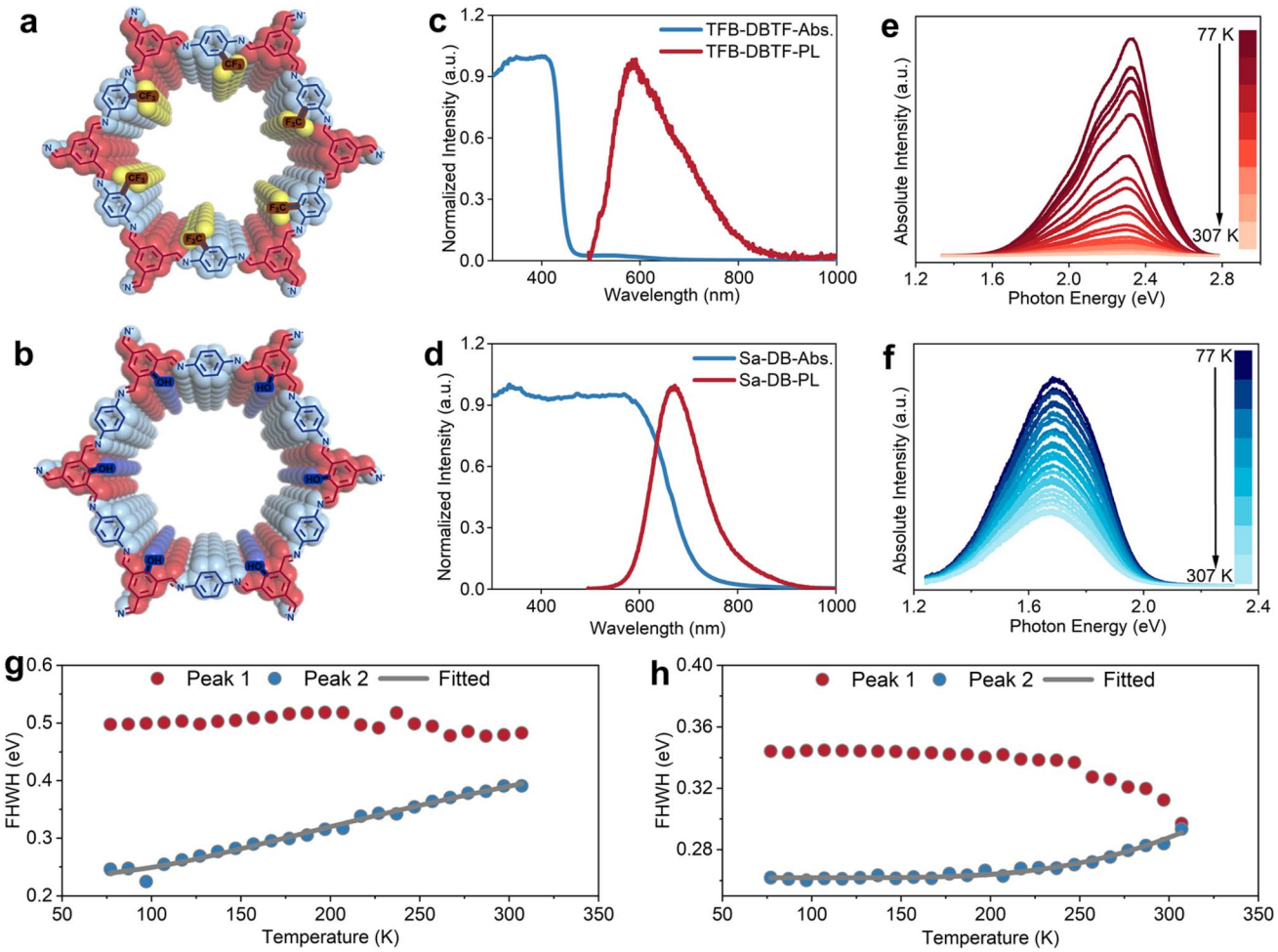

Fig. 2 Molecular structure and spectroscopic characterization of 2D TFB-DB COFs functionalized with trifluoromethyl and hydroxyl groups. (a and b) Molecular structures; (c and d) diffuse reflectance (DR) UV-vis and PL spectra; (e and f) temperature-dependent steady-state PL spectra; (g and h) temperature-dependent FWHM of three representative PL peaks for the COFs with trifluoromethyl and hydroxyl substitution, respectively. The solid gray lines represent fits to the Fröhlich polaronic broadening model, accounting for both inhomogeneous broadening and Fröhlich coupling with LO phonons.

increasing the bandgap (Fig. S4 and S5), whereas the hydroxyl group markedly broadens the absorption range, leading to a pronounced bandgap reduction. This observation further indicates that absorption beyond 400 nm mainly arises from the extended conjugation between the imine linkage and benzene ring within the in-plane framework, which predominantly determines the final bandgap of 2D COFs. Photoluminescence (PL) measurements provide additional insight. The trifluoromethyl group broadens the PL peak of TFB-DB and induces a more prominent Stokes shift (Fig. S13), while the hydroxyl group sharpens the PL peak and significantly suppresses the Stokes shift (Fig. S14). Remarkably, hydroxyl substitution also enables intense PL emission even under shorter-wavelength excitation, consistent with characteristics of a direct single bandgap. These results suggest that extended in-plane conjugation enhances EPC in electron-deficient states, whereas electron-rich states tend to weaken this interaction. This interpretation is further corroborated by temperature-dependent PL results (Fig. 2e and f), where the FWHM of the interlayer PL peak of TFB-DB increases substantially with temperature (~150 meV), in sharp contrast to the much smaller broadening observed for Sa-DB (~40 meV, Fig. 2g and h). Overall, the introduction of side groups with distinct polarities provides a simple yet powerful strategy to tune the bandgap of 2D imine-linked COFs. Beyond bandgap engineering, these substituents also modulate the electron cloud density within the in-plane conjugated framework, thereby influencing the strength of EPC.

Subsequently, we synthesized β-ketoenamine-linked 2D COFs TP-DB (Fig. 3a and S15a) through an aqueous-based strategy to further examine how different covalent linkages influence the electronic structure of 2D COFs.[36] In parallel, we prepared 2D TP-DB modified with trifluoromethyl side groups (Fig. 3b and S16a) to assess the effect of side group polarity. The DR UV-vis absorption spectra reveal that, in addition to the interlayer π–π conjugation absorption peak below 400 nm, two distinct absorption bands emerge beyond 400 nm (Fig. 3c). These features are primarily assigned to in-plane conjugation

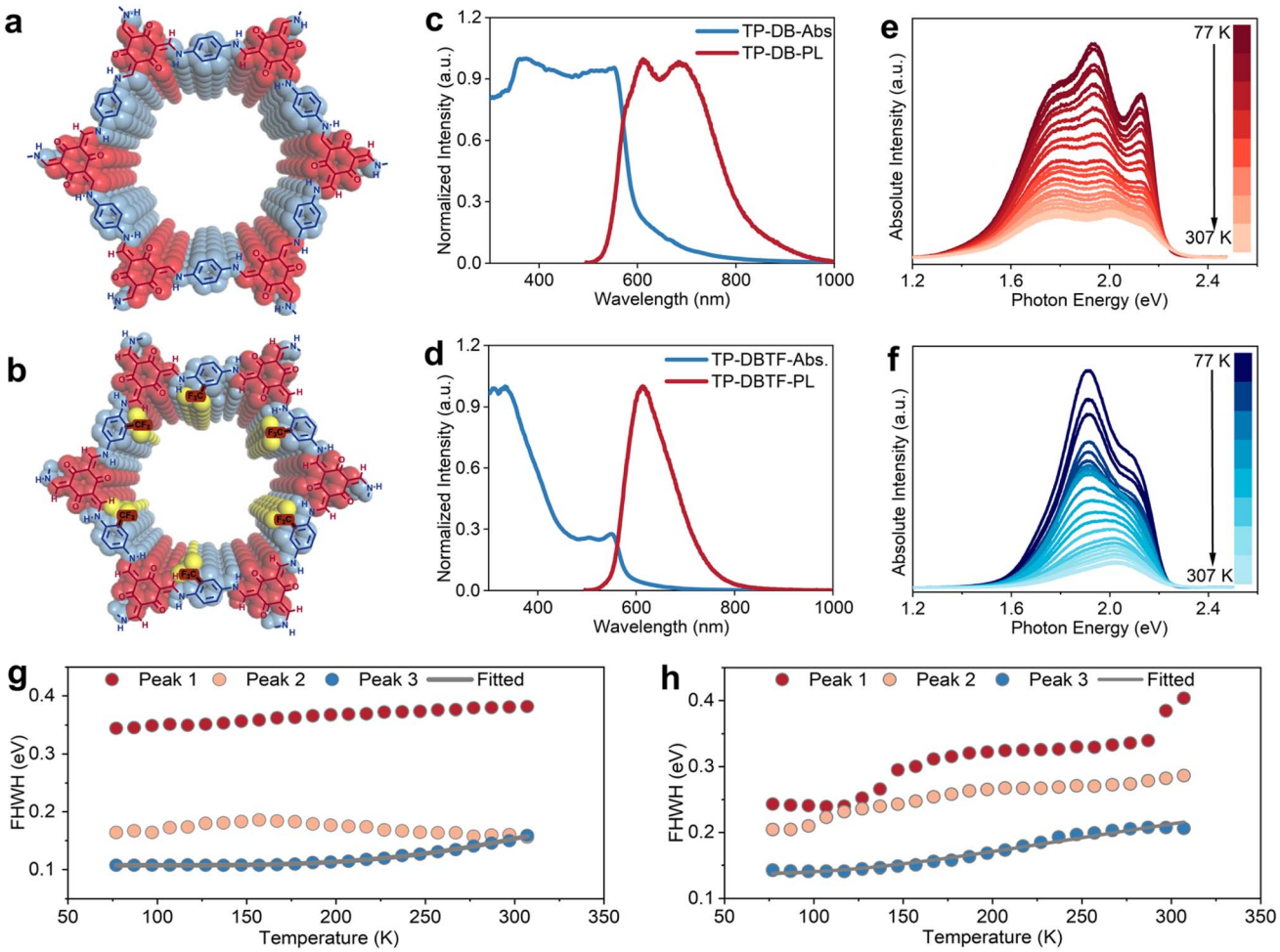

Fig. 3 Molecular structure and spectroscopic characterization of 2D TP-DB COFs with and without trifluoromethyl substitution. (a and b) Molecular structures; (c and d) diffuse reflectance (DR) UV-vis and PL spectra; (e and f) temperature-dependent steady-state PL spectra; (g and h) temperature-dependent FWHM of three representative PL peaks for COFs with and without trifluoromethyl groups, respectively. The solid gray lines represent fits to the Fröhlich polaronic broadening model, accounting for contributions from both inhomogeneous broadening and Fröhlich coupling with LO phonons.

modes in 2D TP-DB, including the n–π conjugation extension between the nitrogen lone pair and the benzene ring and the π–π conjugation extension between the carbonyl and the ethylene bond. The absorption range is broader than that of the amine-linked 2D COFs (TFB-DB), reflecting a higher degree of in-plane conjugation. Moreover, the absorption edge of 2D TP-DB displays two distinct attenuation stages, a more pronounced characteristic that points to the coexistence of direct and indirect bandgaps. This interpretation is also supported by excitation spectra results (Fig. S17a). The introduction of the electron-withdrawing trifluoromethyl group narrows the in-plane absorption range and reduces the absorption intensity of in-plane conjugation (Fig. 3d). This effect likely arises from the weaker electronic interaction of the n–π extended conjugation relative to the π–π extended conjugation in 2D TP-DB, which is more vulnerable to the modulation of the side group electron cloud distribution. Nonetheless, the influence of electron-withdrawing side groups on the electronic structure follows a trend consistent with that observed in amine-linked 2D COFs and results in an increased bandgap in 2D TP-DBTF.

Using the same method, we collected temperature-dependent PL spectra for both β-ketoenamine-linked 2D TP-DB samples (Fig. 3e and f). Compared with the spectra at room temperature, the three PL peaks become more pronounced at low temperatures, particularly the high-energy PL peak that is associated with interlayer π–π relaxation excitation (Peak 3). Furthermore, the PL peaks of 2D TP-DB at low temperatures exhibit a clear overall redshift relative to those at room temperature. These observations provide convincing evidence of EPC in 2D TP-DB. At low temperatures, lattice vibrations are restricted and phonon density decreases, which enhances electronic radiative relaxation and lowers the transition energy between excited and ground states, resulting in a redshift of the PL peak (Fig. S17). We also found that with increasing temperature, the FWHM of the interlayer PL peak expands, a behavior characteristic of Fröhlich interaction that suggests coupling between excitons and longitudinal optical phonons (Fig. 3g). The presence of the electron-withdrawing trifluoromethyl group further amplifies this broadening of the FWHM, implying stronger EPC (Fig. 3h and S18). The calculated

Fröhlich coupling constants of 2D TP-DB and TP-DBTF are significantly larger than those of imine-linked 2D COFs, which can be ascribed to the smaller layer spacing of β-ketoenamine-linked 2D COFs, as confirmed by XRD analysis (Fig. S15 and S16). Interestingly, the FWHM of the PL peak does not vary monotonically with temperature. It first broadens and then narrows as the temperature rises, with the transition occurring near 150 K. This feature likely indicates a shift in the dominant phonon scattering mechanism. At lower temperatures, rising thermal energy enhances molecular vibrations and broadens the emission.[37–39] At higher temperatures, exciton delocalization within the intralayer conjugated network becomes more prominent, producing spectral narrowing due to the suppression of molecular vibrations.[40–42] Fitting the interlayer PL FWHM with the Fröhlich polaronic broadening model demonstrates enhanced coupling between electrons and longitudinal optical phonons above the transition temperature, suggesting that thermal excitation of high-frequency optical phonons governs this process.

Based on the above findings, the PL spectra of the six distinct COFs consistently display significant broadening of the interlayer emission peak with increasing temperature, confirming the presence of EPC behavior. In contrast, the intralayer emission bandwidth remains nearly unchanged across the tested thermal range. We applied the Fröhlich polaronic broadening formula to calculate both the Fröhlich coupling constant and phonon energy (Table S3), thereby quantifying EPC strength in different 2D COF molecular frameworks. To further validate this analysis, we measured the fluorescence decay lifetimes of the six 2D COFs and correlated them with EPC intensity (Fig. S19). The results indicate an intrinsic relationship between the degree of conjugation in covalently bonded molecular structures and the van der Waals-mediated interlayer EPC interactions. For 2D COFs with the same covalent linkage and similar interlayer spacing, the introduction of electron-withdrawing groups reduces the in-plane conjugation, as shown by the narrowing of the extended conjugation absorption range in the spectra, which in turn enhances interlayer EPC, and *vice versa*. By contrast, a reduction in interlayer spacing through covalent bond variation produces a much stronger EPC effect. Unlike the localized polarons commonly observed in traditional organic semiconductors, polarons in 2D COFs display features of long-range polarons along the interlayer direction.[43–45] This characteristic possibly facilitates enhanced charge carrier separation efficiency.[46,47] Nevertheless, stronger EPC may tend to reduce charge carrier mobility, increase non-radiative relaxation pathways, and facilitate recombination, which aligns with the observed decrease in fluorescence lifetime.[48–50] From a molecular design perspective, a controlled decrease in in-plane conjugation or a reduction in interlayer spacing can effectively strengthen interlayer EPC.

Meanwhile, it is important to recognize the inherent limitations of the Fröhlich model, which primarily describes interactions between electrons and longitudinal optical phonons while neglecting contributions from transverse optical and acoustic phonons. We further quantified the temperature-dependent PL broadening by extracting the linear expansion coefficients (dFWHM/dT) for several COF samples. This parameter can also serve as an experimental indicator of electron–phonon coupling strength, and the obtained values (Table S4) follow the same trend as the calculated Fröhlich coupling constants. This consistency reinforces the conclusion that the variations in EPC among these COFs arise from their distinct lattice environments and stacking-dependent vibrational interactions. In the 2D COF systems examined here, the phonon spectrum is complex, comprising both optical and acoustic branches arising from the intricate molecular structures, features that are not captured by the Fröhlich formalism. As a result, this model may underestimate the full complexity of EPC in 2D COFs. Addressing these limitations requires the development of more comprehensive theoretical frameworks that account for electron coupling with multiple phonon branches, including acoustic and transverse optical modes. Such approaches would provide a more complete understanding of EPC in COFs and offer deeper insight into their thermal transport mechanisms. Future studies incorporating these advances are expected to significantly improve both the fundamental understanding and practical exploitation of COF materials in thermal management and related applications.

EPC plays a critical role in determining the thermal conductivity of materials. We synthesized six 2D COF crystal powders and compacted them into bulk plates using cold-compression molding for thermal conductivity measurements (Fig. 4a and S20–S22). To verify the crystallinity of the 2D COFs after compression, synchrotron-based 2D-WAXS measurements were performed on the plate samples. The diffraction patterns exhibit uniform concentric rings, indicative of well-preserved long-range order with random and isotropic orientation after pressing (Fig. 4b). The corresponding 1D profile shows clear (100) and (200) reflections, confirming that the crystallinity is retained despite mechanical processing (Fig. S23). Thermal conductivity measurements of the six 2D COF flakes reveal that their in-plane thermal conductivity generally exceeds 1 W m^{-1} K^{-1} (Fig. 4c and S24–S29), significantly higher than that of conventional organic polymer materials (Table S5). To ensure that the measured values reflect intrinsic properties of well-ordered crystalline 2D COFs, a comparative experiment was conducted using a deliberately low-crystallinity sample (Fig. S30). Subjected to identical cold-pressing and testing protocols, the low-crystallinity sample exhibited thermal conductivity nearly an order of magnitude lower than that of its crystalline counterpart. This comparison underscores the essential role of long-range order in promoting efficient thermal transport and confirms that the high thermal conductivity observed in this study originates from the preserved crystallinity of the COF materials.

More importantly, comparison of thermal conductivity among the six 2D COFs reveals a clear correlation between stronger EPC and higher thermal conductivity (Fig. S31), a trend opposite to that typically observed in conventional organic semiconductors.[51–53] To elucidate the mechanism by which EPC affects thermal conductivity, we performed first-principles calculations of the phonon spectra for two representative 2D COFs, TFB-DB and TP-DB, with differing interlayer EPC

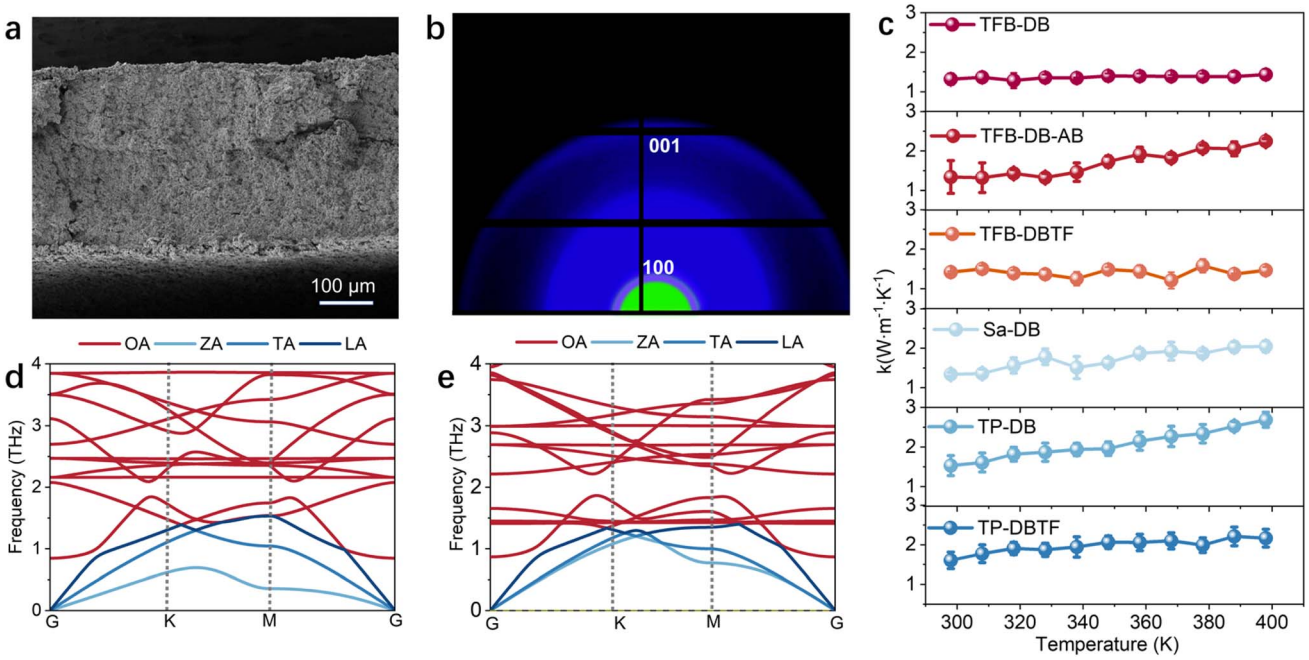

Fig. 4 Thermal conductivity and phonon structures of isotropic 2D COF powder samples. (a) Representative SEM image and (b) 2D-WAXD pattern of a compressed 2D COF pellet. (c) Measured in-plane thermal conductivity of six 2D COF pellets at different temperatures. Calculated in-plane phonon spectra of the (d) 2D TFB-DB COF and (e) 2D TP-DB COF.

strengths (Fig. 4d and e).[54,55] Compared to 2D TFB-DB, 2D TP-DB exhibits pronounced hardening of both in-plane acoustic and optical phonons, resulting in acoustic phonon bunching along the in-plane direction within the first Brillouin zone (Fig. S32). This phenomenon theoretically enhances solid-state heat conduction.[56–58] Additionally, 2D TP-DB displays a larger optical phonon bandgap than 2D TFB-DB, which can suppress Umklapp scattering and improve thermal transport efficiency. Both 2D TFB-DB and TP-DB show no frequency overlap between acoustic and optical phonons, further reducing optical–acoustic phonon scattering and increasing the mean free path of acoustic phonons.

The interlayer EPC-induced in-plane phonon hardening is further supported by Raman spectroscopy. As shown in Fig. S33, 2D TP-DB displays a clear blue shift of several in-plane vibrational modes relative to 2D TFB-DB. This trend is consistent with our phonon dispersion calculations, which show that enhanced interlayer electron–phonon coupling in TP-DB stiffens the low-frequency ZA and LA branches. The agreement between the Raman peak shifts and the calculated phonon hardening provides direct evidence that the interlayer coupling field modulates and elevates the energy of in-plane lattice vibrations. It is acknowledged that crystallinity and defects influence thermal transport, and slight variations are unavoidable because current COF synthesis methods cannot yield samples with fully uniform crystallinity. Nonetheless, the COFs examined here all exhibit comparably high polycrystalline order, making crystallinity-driven differences less dominant. Under these conditions, the consistent trends are most plausibly attributed to variations in electron–phonon coupling rather than to minor differences in crystallinity or grain boundaries. High crystallinity of 2D COFs promotes orderly atomic arrangements, which enhance carrier mobility within the in-plane covalent network.[59–61] Enhanced EPC allows electrons to more effectively screen ionic field effects on phonons, and dynamic polarization and self-energy corrections contribute to the hardening of in-plane acoustic phonons.[62,63] In contrast, interlayer charge transport mainly occurs *via* a hopping mechanism due to interlayer spacing exceeding 3 Å, so EPC tends to increase phonon scattering and limit thermal transport along the interlayer direction.

To experimentally verify the anisotropic thermal conductivity induced by EPC, we fabricated a highly oriented, layered β-ketoenamine-linked 2D COF membrane using a water-based deposition method (Fig. 5a, S34 and S35); detailed procedures are provided in the SI. SEM images reveal that the 2D TP-Bpy COF membranes possess a typical layer-by-layer stacked architecture (Fig. 5b and S36), while 2D WAXS patterns indicate that the sheet-like crystals are highly oriented within the plane (Fig. 5c and S37). Thermal diffusion was measured along both in-plane and cross-plane directions using the laser flash method.[64,65] The results show a nearly two-order magnitude difference in diffusion time (Fig. 5d), and the calculated anisotropy index of thermal conductivity for the oriented 2D TP-Bpy COF films reaches 83.02, markedly higher than that of powder-pressed samples (8.18) (Fig. 5e, f, S38 and S39), directly demonstrating the strong anisotropy arising from directional EPC. Notably, the in-plane thermal conductivity of the oriented film reaches around 20 W m^{-1} K^{-1}. The obtained in-plane thermal conductivity is higher than values recently reported for COF membranes; however, differences in measurement methodologies and the absence of detailed descriptions of the

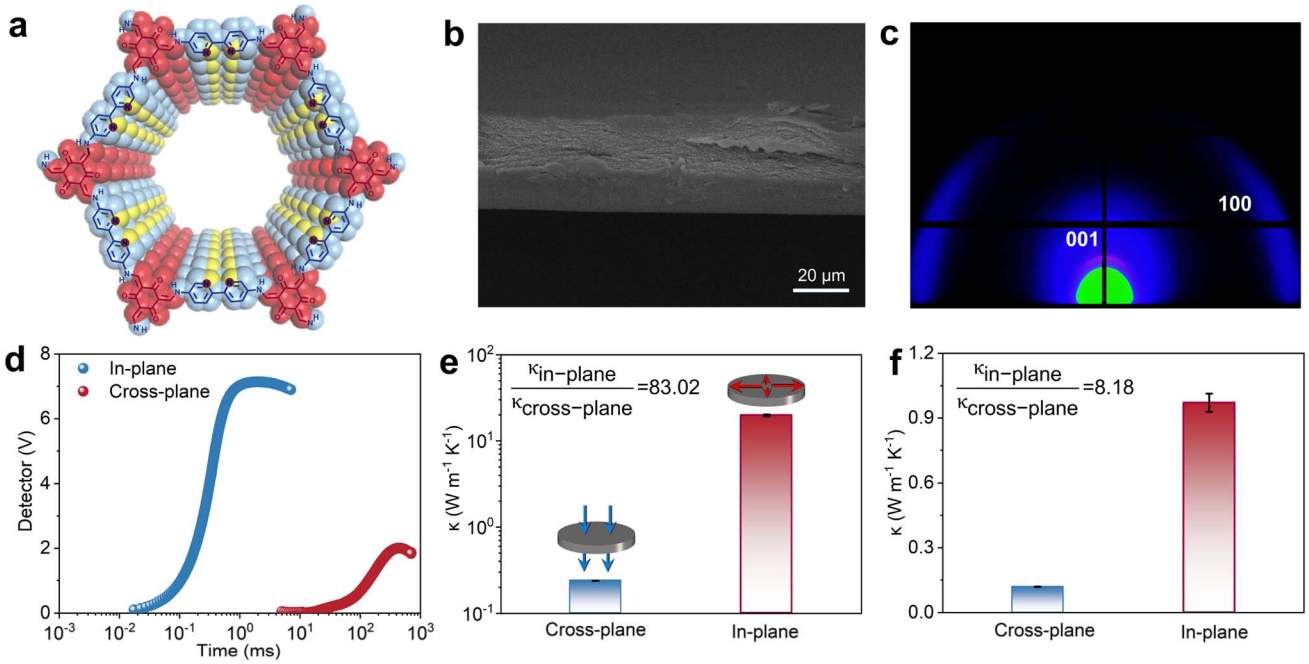

Fig. 5 Thermal conductivity of anisotropic 2D COF thin-film samples. (a) Molecular structure and crystal stacking mode; (b) cross-sectional SEM image; (c) GIWAXD pattern of the 2D TP-Bpy COF; (d) time-dependent laser thermal diffusion signals in the in-plane and cross-plane directions; obtained thermal conductivities of the (e) 2D TP-Bpy COF thin film and (f) 2D TP-Bpy COF pellets prepared from powder.

homemade instruments and data-processing procedures in those studies prevent a direct quantitative comparison. Our measurements were carried out using a commercial laser-flash system operated strictly in accordance with ASTM-based standards. The reliability of this approach is also supported by control experiments on polyethylene and polyimide films of comparable thickness, whose in-plane thermal conductivities remain below 1 W m^{-1} K^{-1} and are fully consistent with literature values, as shown in Fig. S40. This agreement may rule out measurement artifacts as the origin of the high conductivity obtained for the COF films. The SI provides a complete description of the laser-flash protocol, the applied standards, the correction procedures, and the specific considerations required for semiconducting COFs, including the use of a graphite buffer layer to prevent direct laser interaction with the sample surface and the associated photothermal effects. This information enables transparent evaluation and informed discussion within the community. These results highlight the exceptional potential of 2D COFs in thermal management. They also suggest that tailored crystal orientation and EPC strength can enable directional heat transport and high thermal conduction efficiency, providing a foundation for applications in precision thermal management in electronics, spacecraft, batteries, and nanoscale thermal control.

Conclusion

In summary, a comparative investigation of six structurally distinct 2D COFs reveals pronounced anisotropy in EPC. This coupling is primarily along the *c*-axis, stabilized by van der Waals interlayer interactions, and leads to the formation of large polarons through Fröhlich interactions. In contrast, the covalently bonded in-plane *ab*-axis exhibits substantially weaker coupling. A clear relationship exists between in-plane conjugation and interlayer EPC strength, with reduced in-plane conjugation generally enhancing interlayer interactions. This coupling profoundly affects the thermal transport properties of 2D COFs. Along the interlayer direction, EPC promotes frequency overlap between optical and acoustic phonons, which increases phonon scattering and reduces cross-plane thermal conductivity. In-plane, EPC strengthens acoustic phonons, resulting in frequency hardening and phonon bunching that enhance thermal transport. Thermal conductivity measurements of oriented 2D COF thin films demonstrate nearly two orders of magnitude difference between in-plane and cross-plane conductivity, confirming the anisotropic nature of EPC. These findings reveal a unique anisotropy in phonon–electron interactions within 2D COFs, providing new insight into their electron and phonon structures. This work offers a theoretical basis for designing high-performance semiconducting 2D COFs and informs the exploration of their potential in applications requiring precise and efficient thermal management.

Author contributions

S. Zhou proposed and supervised the project, conceptualized and designed the study, performed data analysis and drafted the manuscript. Y. Zhang conducted most of the experiments and theoretical calculations. Z. Dai, Z. Tan, and H. Yang carried out material characterization. All authors contributed to the discussion of results and the preparation of the final manuscript.

Conflicts of interest

The authors declare no competing interests.

Data availability

The data supporting this article have been included as part of the supplementary information (SI). Supplementary information is available. See DOI: https://doi.org/10.1039/d5sc08033a.

Acknowledgements

The authors gratefully acknowledge financial support from the National Natural Science Foundation of China (Grant No. 52503041), the National Science and Technology Major Project of the Ministry of Science and Technology of China (Grant No. 2025ZD0619201), the Sichuan Provincial Department of Science and Technology (Grant No. 2025YFHZ0186), the Fundamental Research Funds for the Central Universities of China (Grant No. 1082204112H83 and 20822041J4076), the Starting Grant of Ministry of Education of China (Grant No. 0082204153346), the Fellowship Grant of China Postdoctoral Science Foundation (Grant No. 2024M762211), and the Outstanding Young Scientists Fund from the State Key Laboratory of Advanced Polymer Materials (Grant No. sklpme2024-2-16 and sklpme2024-2-20). The authors also appreciate the assistance of the Analysis & Testing Center at Sichuan University with spectroscopy data collection. In addition, we also gratefully acknowledge the support of Beamline BL16B at the Shanghai Synchrotron Radiation Facility (SSRF) for WAXD measurements and data analysis.

References

1 H. L. Nguyen, N. Hanikel, S. J. Lyle, C. Zhu, D. M. Proserpio and O. M. Yaghi, A Porous Covalent Organic Framework with Voided Square Grid Topology for Atmospheric Water Harvesting, *J. Am. Chem. Soc.*, 2020, **142**(5), 2218–2221.
2 P. J. Waller, F. Gándara and O. M. Yaghi, Chemistry of Covalent Organic Frameworks, *Acc. Chem. Res.*, 2015, **48**(12), 3053–3063.
3 P. Pachfule, A. Acharjya, J. Roeser, T. Langenhahn, M. Schwarze, R. Schomäcker, A. Thomas and J. Schmidt, Diacetylene Functionalized Covalent Organic Framework (COF) for Photocatalytic Hydrogen Generation, *J. Am. Chem. Soc.*, 2018, **140**(4), 1423–1427.
4 K. T. Tan, S. Ghosh, Z. Y. Wang, F. X. Wen, D. Rodríguez-San-Miguel, J. Feng, N. Huang, W. Wang, F. Zamora, X. L. Feng, A. Thomas and D. L. Jiang, Covalent organic frameworks, *Nat. Rev. Methods Primers*, 2023, **3**(1), 1.
5 M. S. Lohse and T. Bein, Covalent organic frameworks: structures, synthesis, and applications, *Adv. Funct. Mater.*, 2018, **28**(33), 1705553.
6 S. S. Han, H. Furukawa, O. M. Yaghi and W. A. Goddard III, Covalent Organic Frameworks as Exceptional Hydrogen Storage Materials, *J. Am. Chem. Soc.*, 2008, **130**(35), 11580–11581.
7 M. X. Wu and Y. W. Yang, Applications of covalent organic frameworks (COFs): From gas storage and separation to drug delivery, *Chin. Chem. Lett.*, 2017, **28**(6), 1135–1143.
8 H. Fan, A. Mundstock, A. Feldhoff, A. Knebel, J. Gu, H. Meng and J. Caro, Covalent Organic Framework–Covalent Organic Framework Bilayer Membranes for Highly Selective Gas Separation, *J. Am. Chem. Soc.*, 2018, **140**(32), 10094–10098.
9 H. W. Fan, A. Mundstock, A. Feldhoff, A. Knebel, J. H. Gu, H. Meng and J. Caro, Covalent Organic Framework-Covalent Organic Framework Bilayer Membranes for Highly Selective Gas Separation, *J. Am. Chem. Soc.*, 2018, **140**(32), 10094–10098.
10 J. Guo and D. Jiang, Covalent Organic Frameworks for Heterogeneous Catalysis: Principle, Current Status, and Challenges, *ACS Cent. Sci.*, 2020, **6**(6), 869–879.
11 Z. Li, Y. Li, H. Cheng, Y. Song, Y. Jiao, S. Shi, J. Gao, L. Sun and J. Hou, Atomically dispersed Ni active sites on covalent organic frameworks for heterogeneous metallaphotocatalytic C–N cross-coupling, *Appl. Catal. B Environ. Energy*, 2024, **345**, 123698.
12 D. Blätte, F. Ortmann and T. Bein, Photons, Excitons, and Electrons in Covalent Organic Frameworks, *J. Am. Chem. Soc.*, 2024, **146**(47), 32161–32205.
13 Y. Chen and D. Jiang, Photocatalysis with Covalent Organic Frameworks, *Acc. Chem. Res.*, 2024, **57**(21), 3182–3193.
14 M. Y. Zhang, J. K. Li, R. Wang, S. N. Zhao, S. Q. Zang and T. C. Mak, Construction of core–shell MOF@ COF hybrids with controllable morphology adjustment of COF shell as a novel platform for photocatalytic cascade reactions, *Adv. Sci.*, 2021, **8**(19), 2101884.
15 Q. Yang, M. Luo, K. Liu, H. Cao and H. Yan, Covalent organic frameworks for photocatalytic applications, *Appl. Catal., B*, 2020, **276**, 119174.
16 Q. Liu, Q. Li, Y. Li, T. Su, B. Hou, Y. Zhao and Y. Xu, Two-dimensional Covalent Organic Frameworks in Organic Electronics, *Angew. Chem., Int. Ed.*, 2025, **64**(22), e202502536.
17 N. Huang, P. Wang and D. Jiang, Covalent organic frameworks: a materials platform for structural and functional designs, *Nat. Rev. Mater.*, 2016, **1**(10), 1–19.
18 K. Geng, T. He, R. Liu, S. Dalapati, K. T. Tan, Z. Li, S. Tao, Y. Gong, Q. Jiang and D. Jiang, Covalent Organic Frameworks: Design, Synthesis, and Functions, *Chem. Rev.*, 2020, **120**(16), 8814–8933.
19 S.-Y. Ding, J. Gao, Q. Wang, Y. Zhang, W.-G. Song, C.-Y. Su and W. Wang, Construction of Covalent Organic Framework for Catalysis: Pd/COF-LZU1 in Suzuki–Miyaura Coupling Reaction, *J. Am. Chem. Soc.*, 2011, **133**(49), 19816–19822.
20 L. Wang, L. Zhang, B. Lin, Y. Zheng, J. Chen, Y. Zheng, B. Gao, J. Long and Y. Chen, Activation of carbonyl oxygen sites in β-ketoenamine-linked covalent organic frameworks *via* cyano conjugation for efficient photocatalytic hydrogen evolution, *Small*, 2021, **17**(24), 2101017.
21 W. Zhao, P. Yan, H. Yang, M. Bahri, A. M. James, H. Chen, L. Liu, B. Li, Z. Pang and R. Clowes, Using sound to synthesize covalent organic frameworks in water, *Nat. Synth.*, 2022, **1**(1), 87–95.

22 X. Yang, Q. An, X. Li, Y. Fu, S. Yang, M. Liu, Q. Xu and G. Zeng, Charging modulation of the pyridine nitrogen of covalent organic frameworks for promoting oxygen reduction reaction, *Nat. Commun.*, 2024, **15**(1), 1889.

23 K. Wang, Y. Zhong, W. Dong, Y. Xiao, S. Ren and L. Li, Intermediate formation of macrocycles for efficient crystallization of 2D covalent organic frameworks with enhanced photocatalytic hydrogen evolution, *Angew. Chem., Int. Ed.*, 2023, **62**(30), e202304611.

24 L. Hao, R. Shen, C. Huang, Z. Liang, N. Li, P. Zhang, X. Li, C. Qin and X. Li, Fluorenone-based covalent organic frameworks with efficient exciton dissociation and well-defined active center for remarkable photocatalytic hydrogen evolution, *Appl. Catal., B*, 2023, **330**, 122581.

25 B. Bao, R. Li, Y. Hao, R. Xiao, C. Hou, Y. Li, Q. Zhang, K. Li and H. Wang, Tuning Electron Transfer in Pyrene-Based Two Dimensional Covalent Organic Frameworks: Unveiling the Impact of Semi-isomerism on Physicochemical Properties, *Chem. Mater.*, 2024, **36**(6), 2880–2887.

26 J. Tauc, R. Grigorovici and A. Vancu, Optical properties and electronic structure of amorphous germanium, *Phys. Status Solidi B*, 1966, **15**(2), 627–637.

27 X. Ma, Y. Fu, A. Portniagin, N. Yang, D. Liu, A. L. Rogach, J.-G. Dai and D. Lei, Effects of Stokes shift and Purcell enhancement on fluorescence-assisted radiative cooling, *J. Mater. Chem. A*, 2022, **10**(37), 19635–19640.

28 F. Corsini, A. Nitti, E. Tatsi, G. Mattioli, C. Botta, D. Pasini and G. Griffini, Large-area semi-transparent luminescent solar concentrators based on large Stokes shift aggregation-induced fluorinated emitters obtained through a sustainable synthetic approach, *Adv. Opt. Mater.*, 2021, **9**(16), 2100182.

29 R. Zhou, L. Sui, X. Liu, K. Liu, D. Guo, W. Zhao, S. Song, C. Lv, S. Chen and T. Jiang, Multiphoton excited singlet/triplet mixed self-trapped exciton emission, *Nat. Commun.*, 2023, **14**(1), 1310.

30 K. Chen, B. Chen, L. Xie, X. Li, X. Chen, N. Lv, K. Zheng, Z. Liu, H. Pi and Z. Lin, Organic–inorganic copper halide compound with a near-unity emission: large-scale synthesis and diverse light-emitting applications, *Adv. Funct. Mater.*, 2024, **34**(10), 2310561.

31 A. D. Wright, C. Verdi, R. L. Milot, G. E. Eperon, M. A. Pérez-Osorio, H. J. Snaith, F. Giustino, M. B. Johnston and L. M. Herz, Electron–phonon coupling in hybrid lead halide perovskites, *Nat. Commun.*, 2016, 7(1), 11755.

32 J. H. Zhao, X. Mu, L. Wang, Z. Fang, X. Zou and J. Cao, Homogeneously large polarons in aromatic passivators improves charge transport between perovskite grains for> 24% efficiency in photovoltaics, *Angew. Chem., Int. Ed.*, 2022, **61**(14), e202116308.

33 J. H. Burroughes, D. D. Bradley, A. Brown, R. Marks, K. Mackay, R. H. Friend, P. L. Burns and A. B. Holmes, Light-emitting diodes based on conjugated polymers, *nature*, 1990, **347**(6293), 539–541.

34 S. Moser, L. Moreschini, J. Jaćimović, O. S. Barišić, H. Berger, A. Magrez, Y. J. Chang, K. S. Kim, A. Bostwick and E. Rotenberg, Tunable polaronic conduction in anatase TiO 2, *Phys. Rev. Lett.*, 2013, **110**(19), 196403.

35 W. H. Sio and F. Giustino, Polarons in two-dimensional atomic crystals, *Nat. Phys.*, 2023, **19**(5), 629–636.

36 B. P. Biswal, S. Chandra, S. Kandambeth, B. Lukose, T. Heine and R. Banerjee, Mechanochemical Synthesis of Chemically Stable Isoreticular Covalent Organic Frameworks, *J. Am. Chem. Soc.*, 2013, **135**(14), 5328–5331.

37 Y. Li, G. V. Baryshnikov, F. Siddique, P. Wei, H. Wu and T. Yi, Vibration-Regulated Multi-State Long-Lived Emission from Star-Shaped Molecules, *Angew. Chem., Int. Ed.*, 2022, **61**(48), e202213051.

38 C.-Y. Liu, X.-R. Chen, H.-X. Chen, Z. Niu, H. Hirao, P. Braunstein and J.-P. Lang, Ultrafast luminescent light-up guest detection based on the lock of the host molecular vibration, *J. Am. Chem. Soc.*, 2020, **142**(14), 6690–6697.

39 C.-Y. Liu, H.-F. Wang, Z.-G. Ren, P. Braunstein and J.-P. Lang, Fine-tuning of luminescence through changes in Au–S bond lengths as a function of temperature or solvent, *Inorg. Chem.*, 2019, **58**(13), 8533–8540.

40 T. Shi, H. E. Jackson, L. M. Smith, N. Jiang, H. H. Tan and C. Jagadish, Thermal delocalization of excitons in GaAs/AlGaAs quantum well tube nanowires, *Nano Lett.*, 2016, **16**(2), 1392–1397.

41 D. Chtchekine, G. Gilliland, Z. Feng, S. Chua, D. Wolford, S. Ralph, M. Schurman and I. Ferguson, Temperature dependence of bound exciton emissions in GaN, *MRS Internet J. Nitride Semicond. Res.*, 1999, **4**, 733–738.

42 S. Peng, Q. Wei, B. Wang, Z. Zhang, H. Yang, G. Pang, K. Wang, G. Xing, X. W. Sun and Z. Tang, Suppressing strong exciton–phonon coupling in blue perovskite nanoplatelet solids by binary systems, *Angew. Chem., Int. Ed.*, 2020, **59**(49), 22156–22162.

43 J. L. Bredas and G. B. Street, Polarons, bipolarons, and solitons in conducting polymers, *Acc. Chem. Res.*, 1985, **18**(10), 309–315.

44 D. A. Stanfield, Z. Mehmedović and B. J. Schwartz, Vibrational Stark Effect Mapping of Polaron Delocalization in Chemically Doped Conjugated Polymers, *Chem. Mater.*, 2021, **33**(21), 8489–8500.

45 R. Ghosh and F. C. Spano, Excitons and Polarons in Organic Materials, *Acc. Chem. Res.*, 2020, **53**(10), 2201–2211.

46 H. Li, R. Chen, L. Sun, Y. Wang, Q. Liu, Q. Zhang, C. Xiao and Y. Xie, Hole Polaron-Mediated Suppression of Electron–Hole Recombination Triggers Efficient Photocatalytic Nitrogen Fixation, *Adv. Mater.*, 2024, **36**(44), 2408778.

47 F. Provencher, N. Bérubé, A. W. Parker, G. M. Greetham, M. Towrie, C. Hellmann, M. Côté, N. Stingelin, C. Silva and S. C. Hayes, Direct observation of ultrafast long-range charge separation at polymer–fullerene heterojunctions, *Nat. Commun.*, 2014, **5**(1), 4288.

48 H. Mai, X. Wen, X. Li, N. S. Dissanayake, X. Sun, Y. Lu, T. C. Le, S. P. Russo, D. Chen and D. A. Winkler, Data driven high quantum yield halide perovskite phosphors design and fabrication, *Mater. Today*, 2024, **74**, 12–21.

49 L. M. Herz, Charge-Carrier Mobilities in Metal Halide Perovskites: Fundamental Mechanisms and Limits, *ACS Energy Lett.*, 2017, **2**(7), 1539–1548.
50 L. Ni, U. Huynh, A. Cheminal, T. H. Thomas, R. Shivanna, T. F. Hinrichsen, S. Ahmad, A. Sadhanala and A. Rao, Real-Time Observation of Exciton–Phonon Coupling Dynamics in Self-Assembled Hybrid Perovskite Quantum Wells, *ACS Nano*, 2017, **11**(11), 10834–10843.
51 X. Qian, J. Zhou and G. Chen, Phonon-engineered extreme thermal conductivity materials, *Nat. Mater.*, 2021, **20**(9), 1188–1202.
52 J. Ordonez-Miranda, J. Alvarado-Gil and R. Yang, Effect of the electron–phonon coupling on the effective thermal conductivity of metallic bilayers, *Int. J. Thermophys.*, 2013, **34**, 1817–1827.
53 B. Liao, B. Qiu, J. Zhou, S. Huberman, K. Esfarjani and G. Chen, Significant Reduction of Lattice Thermal Conductivity by the Electron–Phonon Interaction in Silicon with High Carrier Concentrations: A First-Principles Study, *Phys. Rev. Lett.*, 2015, **114**(11), 115901.
54 Z. Pan, X. Huang, Y. Fan, S. Wang, Y. Liu, X. Cong, T. Zhang, S. Qi, Y. Xing, Y.-Q. Zheng, *Atomic-precision non-van der waals 2D structures: superconductivity in π–d conjugated coordination polymers*, 2024.
55 T. Tadano and S. Tsuneyuki, Self-consistent phonon calculations of lattice dynamical properties in cubic SrTiO 3 with first-principles anharmonic force constants, *Phys. Rev. B*, 2015, **92**(5), 054301.
56 S. Thakur and A. Giri, Origin of Ultralow Thermal Conductivity in Metal Halide Perovskites, *ACS Appl. Mater. Interfaces*, 2023, **15**(22), 26755–26765.
57 B. Wei, X. Zhang, W. Li, J. Li, Y. Li, Q. Gao, J. Hong, C.-W. Nan and Y.-H. Lin, Optical phonons on thermal conduction in advanced materials, *Appl. Phys. Rev.*, 2025, **12**(1), 011324.
58 X. Meng, T. Pandey, J. Jeong, S. Fu, J. Yang, K. Chen, A. Singh, F. He, X. Xu and J. Zhou, Thermal conductivity enhancement in MoS 2 under extreme strain, *Phys. Rev. Lett.*, 2019, **122**(15), 155901.
59 S. Fu, E. Jin, H. Hanayama, W. Zheng, H. Zhang, L. Di Virgilio, M. A. Addicoat, M. Mezger, A. Narita, M. Bonn, K. Müllen and H. I. Wang, Outstanding Charge Mobility by Band Transport in Two-Dimensional Semiconducting Covalent Organic Frameworks, *J. Am. Chem. Soc.*, 2022, **144**(16), 7489–7496.
60 S. Seki, R. P. Paitandi, W. Choi, S. Ghosh and T. Tanaka, Electron Transport over 2D Molecular Materials and Assemblies, *Acc. Chem. Res.*, 2024, **57**(18), 2665–2677.
61 Y. Zhu, S. Jiang, X. Jing and X. Feng, Electrically conductive 2D covalent organic frameworks, *Trends Chem.*, 2022, **4**(2), 128–141.
62 P. T. Araujo, D. L. Mafra, K. Sato, R. Saito, J. Kong and M. S. Dresselhaus, Phonon Self-Energy Corrections to Nonzero Wave-Vector Phonon Modes in Single-Layer Graphene, *Phys. Rev. Lett.*, 2012, **109**(4), 046801.
63 H. Miao, T. Zhang, H. Li, G. Fabbris, A. Said, R. Tartaglia, T. Yilmaz, E. Vescovo, J.-X. Yin and S. Murakami, Signature of spin-phonon coupling driven charge density wave in a kagome magnet, *Nat. Commun.*, 2023, **14**(1), 6183.
64 W. N. dos Santos, P. Mummery and A. Wallwork, Thermal diffusivity of polymers by the laser flash technique, *Polym. Test.*, 2005, **24**(5), 628–634.
65 M. Li and M. Akoshima, Appropriate metallic coating for thermal diffusivity measurement of nonopaque materials with laser flash method and its effect, *Int. J. Heat Mass Transfer*, 2020, **148**, 119017.